Material interface effects on the topology optimization of multi-phase structures using a level set method

Natasha Vermaak, Georgios Michailidis, Guillaume Parry, Raphael Estevez, Grégoire Allaire, Yves Brechet

Material interface effects on the topology optimization of multi-phase structures using a level set method

Natasha Vermaak · Georgios Michailidis · Guillaume Parry · Rafael Estevez · Grégoire Allaire · Yves Bréchet

Abstract A level set method is used as a framework to study the effects of including material interface properties in the optimization of multi-phase elastic and thermoelastic structures. In contrast to previous approaches, the material properties do not have a discontinuous change across the interface that is often represented by a sharp geometric boundary between material regions. Instead, finite material interfaces with monotonic and non-monotonic property variations over a physically motivated interface zone are investigated. Numerical results are provided for several 2D problems including compliance and displacement minimization of structures composed of two and three materials. The results highlight the design performance changes attributed to the presence of the continuously graded material interface properties.

N. Vermaak · G. Parry · Y. Bréchet
SIMaP-Université de Grenoble, INPG, 1130 rue de la Piscine
B.P. 75, 38402 St. Martin d'Héres, Cedex, France
e-mail: Natasha.Vermaak@simap.grenoble-inp.fr

G. Michailidis · G. Allaire
Centre de Mathématiques Appliquées (UMR 7641),
École Polytechnique, 91128 Palaiseau, France

R. Estevez
SIMaP-Université de Grenoble, UMR 5266 CNRS / INPG / UJF,
1130 rue de la Piscine B.P. 75, 38402 St. Martin d'Héres, Cedex,
France

N. Vermaak (✉)
Mechanical Engineering and Mechanics, Lehigh University,
19 Memorial Drive West, Bethlehem, PA 18015-3085, USA
e-mail: vermaak@lehigh.edu

Keywords Shape optimization · Graded interface · Thermoelastic · Elasticity · Level set method · Multi-material · Multi-phase · Topology

1 Introduction

Recent advances in the development of the level set method for topology optimization (Allaire et al. 2014) have enhanced the treatment of material interfaces, a key feature introduced in multi-phase models that is nevertheless typically ignored. The interfaces of interest are those of dissimilar materials (bi-material) or heterophase boundaries within the classification of solid or bulk interfaces. For this class of interfaces, lattice-parameter changes in the interfacial region, induced by interfacial stresses, may have a pronounced effect on the physical properties and chemical composition at or near the interface (Wolf 1992). The present work seeks to capitalize on these potential property differences. In a variety of fields material interfaces play a pivotal role in the performance of structures, often dictating tolerances and processing choices, lifetime and failure characteristics. Explicitly accounting for interfacial properties beyond a simple interpolation between bulk properties is necessary if one is to take full advantage of incorporating materials science input into optimal shape design methodologies.

The benefits of integrated engineering paradigms that allow simultaneous and cooperative feedback among advanced manufacturing methods and computational modeling – including optimization – have been recently recognized and broadly advised (Committee on Integrated Computational Materials Engineering 2008). Advances in precision and control of additive manufacturing now allow for consideration of interface characteristics in structure

and material design optimization. These advances include techniques such as: 3D printing, laser stereo-lithography and electron beam melting (Pasko et al. 2011; Lipson and Pollack 2000; Ikuta and Hirowatari 1993; Harrysson et al. 2008), along with characterization techniques at the interfacial level such as blister, wedge, and essential work of fracture tests (Braccini and Dupeux 2012). In the present work, only elastic and thermoelastic structural optimization will be considered but the application to material design is forthcoming.

Multi-phase topology optimization for problems of elastic and thermoelastic structures and materials design has been widely studied within the framework of the homogenization method (Allaire et al. 1997; Bendsoe and Kikuchi 1988) and its variants, such as the Solid Isotropic Material with Penalization (SIMP) method (Bendsoe and Sigmund 1999, 2004). This topic has also been explored (Wang et al. 2004) using the level set method for shape and topology optimization (Allaire et al. 2004; Wang et al. 2003). The level set method was originally developed by Osher and Sethian (1988) for numerically tracking fronts and free boundaries. The level set method is extremely versatile, used in many fields including fluid mechanics and image processing, and is computationally very efficient. Previously, multi-phase or multi-material topology optimization of structures using the level set method has been performed for problems of compliance only (Allaire et al. 2014; Wang and Wang 2004) and thermoelastic structural problems have utilized only one material (and voids) (Xia and Wang 2008b; Laszczyk 2011).

The level set method has also been applied for optimization problems that incorporate concepts of functionally-graded materials and heterogeneous structures (Wang and Wang 2005; Xia and Wang 2008a). In Wang and Wang (2005), the interface between the different phases in a heterogeneous structure was considered to be a geometrically sharp boundary, but each of the phases was allowed to have graded properties. In contrast, the present work focuses on graded interfaces between isotropic bulk materials. In Wang and Wang (2005), polynomials were used to describe the gradation in properties within a material region and a sensitivity analysis was performed that considered the polynomial coefficients as parameters of the optimization problem. However, numerical results were presented only for piecewise constant materials. In Xia and Wang (2008a), the authors presented a method for the simultaneous optimization of the shape and of the material properties of a structure. They used the level set method for shape and topology optimization. Additionally, a density field was defined in the domain, to account for variation in the material properties, and its distribution was optimized solving the classic "variable thickness sheet" problem.

The enabling theory for the account of material interface effects in the level set methodology of topology optimization has already been presented in a rigorous mathematical framework in Allaire et al. (2014) and will be summarized below. This theory allows the designer to replace the ideal and mathematically sharp material interface with a finite and physically meaningful interface transition zone. Previously, including Allaire et al. (2014), this transition zone has employed smoothly-monotonic Heaviside-type interpolation within the transition function. The present work, inspired by a similar choice in thermodynamic modeling presented by the ideal Gibbs interface and the Guggenheim model (Guggenheim 1959) (see Fig. 1), seeks to take advantage of new design possibilities enabled by the interfacial transition zone. In particular, we investigate thermoelastic models and non-monotonic interpolations of the material properties within the transition zone, which were not considered in Allaire et al. (2014).

Interfaces between materials are not neutral: they result often from interdiffusion and reactions between two parent phases. For instance, the interface between two polymers may be the locus for chain reptation and entanglement. The interface between two different steels may lead to carbon diffusion and the creation, after quenching, of a martensitic layer or, conversely, a decarburized layer. The interface between copper and nickel (two elements with full miscibility) will lead to a solid solution. These examples show the variety of situations encompassed by the term "interface." They also indicate that the properties of interest may not be an average of the bulk properties: in general, a martensitic layer has a yield stress higher than the yield stress of the bulk materials, and a decarburized layer has a lower yield stress. Additionally, the electrical and thermal conductivity of a solid solution is lower than that of the pure metals (such as copper and nickel). Therefore, using the interfacial properties as an input in the design of optimal structures requires the consideration of non-monotonic transition functions within the interface that exhibit maxima or minima with respect to the bulk material values.

Depending on processing and manufacturing conditions, finite interface zones with smooth monotonic and non-monotonic interface property transitions can be promoted. The engineering of these transition zones profits from the mature studies of functionally graded materials (Miyamoto

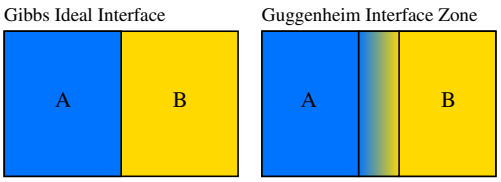

Fig. 1 Classic models for material interfaces: Gibbs ideal sharp interface (*left*) and Guggenheim smooth or graded interface zone (*right*)

et al. 1999; Xia and Wang 2008a; Mello and Silva 2013) and advances in polymer science (Creton et al. 2002) among many others. Non-smooth (not C-1 continuous) non-monotonic interface properties are also possible (Simar et al. 2012), but the non-smoothness of such transitions poses an additional difficulty for the numerical fixed-mesh approximation and are thus not addressed herein. Nevertheless, the introduction of smooth non-monotonic transition functions over a finite interface zone allows for properties that differ, sometimes markedly, from that of the bulk materials alone.

The article is organized in the following way. First, the background and use of the level set approach for topological optimization is described. The description and influence of additional parameters related to interface properties are also introduced. In the second section, the optimization protocol is used on some benchmark problems in 2D under plane stress conditions. These problems involve the compliance minimization of multi-material elastic structures and also displacement minimization in thermoelastic structures. The restriction to 2D is without loss of generality as the ease of extension to 3D is one of the benefits of the level set method (Allaire et al. 2004).

2 Topological optimization

There are many topology optimization methods that address the optimal distribution of materials in a fixed working domain in order to minimize an objective related to overall mechanical behavior or cost (Eschenauer and Olhoff 2001; Bendsoe and Sigmund 2004). For example, density approaches are based on a fixed mesh of the design domain, D (Fig. 2), wherein a density field is defined. The objective function is evaluated by solving the physical equations with material properties that depend on the density field by following an interpolation scheme that specifies how, for example, the elastic modulus tensor varies from that of the constitutive material when the density value is 1, to zero when the density is 0. This material interpolation scheme may be fictitious, such as a power law used in the SIMP method (Bendsoe and Sigmund 1999, 2004), or based on Hashin-Strickman bounds derived by the homogenization method (Bendsoe and Sigmund 1999). The optimization is then reduced to a functional optimization with respect to the density function, based on an analytical derivative. At the end of the optimization procedure, a composite solution is obtained with a density between 0 and 1. When composites are not desired, a penalization step is added in order to progressively eliminate the non-physical intermediate values of density. The main disadvantage of these density approaches is that the obtained optimized shape is strongly sensitive to the density interpolation scheme as well as the penalization method.

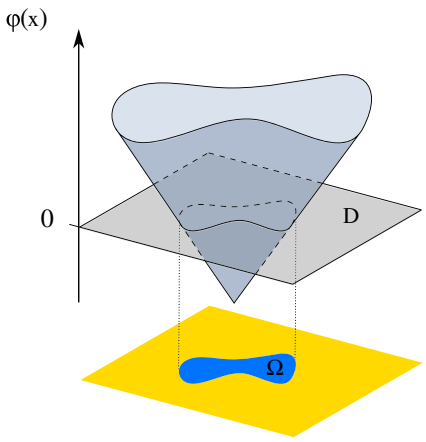

Fig. 2 Schematic level set function, $\phi(x)$, and the corresponding domain, Ω

The level set method is a way to implicitly define the domain, Ω, on a fixed mesh of the design domain, D (Fig. 2). The iterative optimization of the shape is done by advecting the level set function with a velocity field that is found through shape derivation (Allaire et al. 2004; Wang et al. 2003). The transport equation is usually a Hamilton-Jacobi equation (Sethian 1999). Physical equations are solved on the full design domain and voids or pores are mimicked with extremely weak material properties. Sometimes, a smoothed fictitious interface is introduced such as is done in phase field simulations (Wang and Zhou 2004; Zhou and Wang 2007). In 2D, when Hamilton-Jacobi equations are solved using a Courant-Friedrichs-Lewy (CFL) time step restriction, only partial topological changes are allowed. The CFL condition or maximum principle asserts that the numerical waves should propagate at least as fast as the physical waves which ensures that the propogating front crosses no more than one element in one time step (Sethian 1999; Osher and Fedkiw 2002). Indeed, the maximum principle satisfied by this transport equation makes the nucleation of new material during advection impossible. Nevertheless, coarsening of existing inclusions and features can occur, enabling at least partial topological changes. Consequently, initialization of the domain is usually done so that there are a large number of material inclusions or voids. A remedy to this problem is the use of a topological derivative (Sokolowski and Zochowski 1999; Allaire et al. 2005), but it is not included in this work. In the following, the level set method using a Hamilton-Jacobi transport equation is used for the optimization.

The feature common to these methods in their treatment of multiple materials is in their numerical approach to interface modeling. While an exact formulation of the optimization problem would require that disparate material properties be discontinuous at the interface between two materials, it is numerically challenging to incorporate this

discontinuity. As an alternative to including this interface discontinuity, it is general practice to devise an appropriate numerical interpolation scheme to "smooth out" the problem. These material property interpolation schemes can be quite involved (Yin and Ananthasuresh 2002) and much work has been done in exploring their effects from a numerical standpoint (see Allaire et al. 2014 for further discussion). Previously, to the best of the authors' knowledge, only smooth and monotonic interpolation schemes have been employed at the interface. Furthermore, these schemes have been used with an emphasis on numerical application and the ability to penalize (when composites were not desired) fictitious "intermediate" properties or densities that had no physical meaning. The focus of the present work is the reinterpretation of the numerical short-cut of the "smoothed out" interface from a materials perspective that allows new functionality to be derived and exploited in topological optimization and design.

The new generalized level set topology optimization formulation developed in Allaire et al. (2014) extends the applicability of the method to account for the influence of finite interfaces. The focus of Allaire et al. (2014) is to explain why the shape derivatives used in the literature so far for multi-material problems are not correct in full mathematical rigor. They also provide the appropriate theorems for exact shape derivatives with finite interface zones between materials. Futhermore, they demonstrate how these converge to the shape derivatives for mathematically sharp interfaces when a regularized Heaviside function is used for the interpolation scheme and when the interface zone thickness approaches zero. In the following, the application of the generalized finite material interface formulation will be presented in order to study the effects of including physically-motivated interface characteristics under both elastic and thermoelastic conditions.

2.1 Shape optimization of multi-phase structures in thermoelasticity

2.1.1 Setting of the problem

Without loss of generality, the case of two isotropic materials will be described with and without void. A typical case study is defined in which the objective is to optimize the distribution of two materials in a fixed working domain, D, in order to minimize a cost function related to the displacement field. In this work, we consider the maximization of the structure's stiffness by minimizing its total compliance (work done by the loads), as well as the minimization of a target displacement. The structure deforms under a load g applied to a part of its boundary and also due to thermal strain mismatch. The boundary of D is typically comprised of three disjoint parts such that $\partial D = \partial D_0 \cup \Gamma_D \cup \Gamma_N$, where Dirichlet boundary conditions are applied at Γ_D, homogeneous Neumann conditions at ∂D_0 and non-homogeneous Neumann conditions at Γ_N. Instead of a sharp interface between the two materials, an intermediate zone in which the material properties are interpolated is considered (Fig. 3). The width of this zone and the interpolation functions for the material properties are described using the signed-distance function to the intermediate surface $\partial\Omega$ of the two materials. This surface is implicitly defined as the zero level set of a one dimension higher level set function ϕ and seperates the domain into two subdomains Ω and $D\backslash\Omega$; where $D\backslash\Omega$ is the remaining subdomain defined by the absence of Ω from the full domain (Fig. 2). The displacement u is the unique solution of the thermo-elasticity system

$$\begin{cases} -\mathrm{div}\left(A(d_\Omega)\left(e(u)-\alpha(d_\Omega)\Delta T\right)\right) = 0 \text{ in } D, \\ u = 0 \text{ on } \partial\Gamma_D, \\ \big(A(d_\Omega)\left(e(u)-\alpha(d_\Omega)\Delta T\right)\big)n = 0 \text{ on } \partial D_0, \\ \big(A(d_\Omega)\left(e(u)-\alpha(d_\Omega)\Delta T\right)\big)n = g \text{ on } \Gamma_N, \end{cases} \tag{1}$$

where ΔT is the fixed and constant change in temperature, A is the Hooke's tensor, α is the coefficient of thermal expansion (CTE) tensor and d_Ω is the signed-distance function to $\partial\Omega$. The explicit dependence of the coefficients A and α on the distance function d_Ω will be specified in Sections 3.1 and 3.2.

The optimization problem reads

$$\min_{\Omega\in\mathscr{U}ad} J(u(\Omega)) \quad s.t. \int_\Omega dx = V_{tar}, \tag{2}$$

where $u(\Omega)$ is the unique solution of (1), $\mathscr{U}ad$ is a set of admissible shapes (requiring some smoothness), $J(u(\Omega))$ is the objective function and V_{tar} is the target volume for one of the materials occupying the domain Ω.

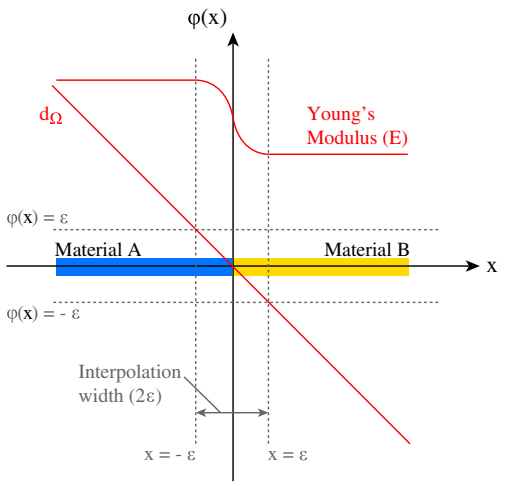

Fig. 3 Numerical approach to model material interfaces with varying properties across the interface

2.1.2 Shape derivative

In order to implement the above equality constraint, an augmented Lagrangian method, suitable for inequality constraints as well, was applied. Inequality constraints were also explored but are not presented herein; see Rao (2009) for details regarding the augmented Lagrangian formulation for inequality constraints. The method of Céa (1986) is used for the formal calculation of the shape derivative. The Lagrangian reads

$$\begin{aligned} L(v,q,\mu) = \; & J(v) \\ & + \int_D -\mathrm{div}\left(A(d_\Omega)\left(e(v)-\alpha(d_\Omega)\Delta T\right)\right)\cdot q\, dx \\ & + \int_{\Gamma_D} \mu \cdot v\, ds \\ & + \int_{\partial D_0} A(d_\Omega)\left(e(v)-\alpha(d_\Omega)\Delta T\right)n \cdot q\, ds \\ & + \int_{\Gamma_N} \left(A(d_\Omega)\left(e(v)-\alpha(d_\Omega)\Delta T\right)n - g\right)\cdot q\, ds \\ & + \lambda a(\Omega) + \tfrac{r}{2}a(\Omega)^2, \end{aligned} \tag{3}$$

where λ, r are scalars to be updated at each iteration so that the volume constraint is satisfied at convergence; v, q, μ are vector-valued functions defined in D (independent of Ω) and

$$a(\Omega) = \int_\Omega dx - V_{tar}. \tag{4}$$

Taking the partial derivative of L with respect to q, in the direction ϕ, which is a given vector-valued function defined in D, and equating this partial derivative to zero at the optimal point u, p, μ^*, results in

$$\int_D -\mathrm{div}\left(A(d_\Omega)\left(e(u)-\alpha(d_\Omega)\Delta T\right)\right)\cdot \phi\, dx = 0, \tag{5}$$

$$\int_{\partial D_0} A(d_\Omega)\left(e(u)-\alpha(d_\Omega)\Delta T\right)n \cdot \phi\, ds = 0, \tag{6}$$

and

$$\int_{\Gamma_N} \left(A(d_\Omega)\left(e(u)-\alpha(d_\Omega)\Delta T\right)n - g\right)\cdot \phi\, ds = 0, \tag{7}$$

and thus

$$-\mathrm{div}\left(A(d_\Omega)\left(e(u)-\alpha(d_\Omega)\Delta T\right)\right) = 0 \quad \text{in } D, \tag{8}$$

$$A(d_\Omega)\left(e(u)-\alpha(d_\Omega)\Delta T\right)n = 0 \quad \text{on } \partial D_0, \tag{9}$$

and

$$A(d_\Omega)\left(e(u)-\alpha(d_\Omega)\Delta T\right)n = g \quad \text{on } \Gamma_N. \tag{10}$$

In the same way, the partial derivative of L with respect to μ results in

$$u = 0 \quad \text{on } \Gamma_D. \tag{11}$$

Equations (8)–(11) show that u is indeed the unique solution of (1). In order to calculate the adjoint state, the Lagrangian is written in the following form

$$\begin{aligned} L(v,q,\mu) = \; & J(v) \\ & + \int_D A(d_\Omega)\, e(v)e(q)\, dx \\ & - \int_D A(d_\Omega)\,\alpha(d_\Omega)\Delta T\, e(q) dx \\ & - \int_{\Gamma_D} A(d_\Omega)\, e(v)\, n\, q\, ds \\ & + \int_{\Gamma_D} A(d_\Omega)\,\alpha(d_\Omega) n\, \Delta T\, q\, ds \\ & - \int_{\Gamma_N} g \cdot q\, ds \\ & + \int_{\Gamma_D} \mu \cdot v\, ds + \lambda a(\Omega) \\ & + \tfrac{r}{2}a(\Omega)^2. \end{aligned} \tag{12}$$

Setting the partial derivative of L with respect to v in the direction ϕ equal to zero, at the optimal point

$$\begin{aligned} J'(v)(\phi) \; & + \int_D A(d_\Omega)\, e(\phi)e(p)\, dx - \int_{\Gamma_D} A(d_\Omega)\, e(\phi)n \cdot p ds \\ & + \int_{\Gamma_D} \mu^* \cdot \phi\, ds = 0 \Rightarrow J'(v)(\phi) \\ & + \int_D -\mathrm{div}\left(A(d_\Omega)e(p)\right)\cdot \phi dx \\ & + \int_{\partial D_0} A(d_\Omega)e(p)n \cdot \phi ds \\ & + \int_{\Gamma_N} A(d_\Omega)e(p)n \cdot \phi ds + \int_{\Gamma_D} A(d_\Omega)e(p)n \cdot \phi ds \\ & - \int_{\Gamma_D} A(d_\Omega)\, e(\phi)n \cdot p + \int_{\Gamma_D} \mu^* \cdot \phi\, ds = 0. \end{aligned} \tag{13}$$

In the case of the compliance, $J(v)$ has the form

$$J(v) = \int_{\Gamma_N} g \cdot v\, ds + \int_D A(d_\Omega)\alpha(d_\Omega)\Delta T\, e(v) dx. \tag{14}$$

Therefore,

$$J'(v)(\phi) = \int_{\Gamma_N} g \cdot \phi\, ds + \int_D A(d_\Omega)\alpha(d_\Omega)\Delta T\, e(\phi) dx, \tag{15}$$

and the following equations are derived

$$\mu^* = -A(d_\Omega)e(p)n, \tag{16}$$

$$p = 0 \quad \text{on } \Gamma_D, \tag{17}$$

$$A(d_\Omega)\left(e(p)-\alpha(d_\Omega)\Delta T\right)n = -g \quad \text{on } \partial\Gamma_N, \tag{18}$$

$$A(d_\Omega)\left(e(p)-\alpha(d_\Omega)\Delta T\right)n = 0 \quad \text{on } \partial D_0, \tag{19}$$

$$-\mathrm{div}\left(A(d_\Omega)\left(e(p)+\alpha(d_\Omega)\Delta T\right)\right) = 0 \quad \text{in } D. \tag{20}$$

Thus $p = -u$ and the problem is said to be self-adjoint. In the case of minimizing the square of the displacement at a target point x_{tar}, we can consider an objective function of the type

$$J(v) = \int_D \delta(x_{tar}) v^2 dx, \tag{21}$$

where $\delta(x_{tar})$ is a Dirac mass function concentrated at point x_{tar}. In this case,

$$J'(v)(\phi) = \int_D \delta(x_{tar}) 2\, v\, \phi\, dx \tag{22}$$

and the equations (17–20) defining the adjoint state, now take the form

$$p = 0 \quad \text{on } \Gamma_D, \tag{23}$$

$$A(d_\Omega)\,(e(p) - \alpha(d_\Omega)\Delta T)n = 0 \quad \text{on } \Gamma_N \cup \partial D_0, \tag{24}$$

$$-\operatorname{div}\left(A(d_\Omega)\,(e(p) + \alpha(d_\Omega)\Delta T)\right) = -\delta(x_{tar}) 2u \quad \text{in } D. \tag{25}$$

Finally, deforming the structure in the direction of a smooth vector field θ (see Allaire et al. (2004) for details), the shape derivative of the objective function is found to be the shape derivative of the Lagrangian at the optimal point

$$J'(u(\Omega))(\theta) = L'(u, p, \mu^*)(\theta), \tag{26}$$

which, after some algebra, for the compliance case results in

$$J'(u(\Omega))(\theta) = \begin{cases} \displaystyle\int_D \frac{\partial d_\Omega}{\partial \Omega}(\theta)\big[2A'(d_\Omega)\alpha(d_\Omega)\Delta T e(u) \\ +2A(d_\Omega)\alpha'(d_\Omega)\Delta T e(u) \\ -A'(d_\Omega)e(u)e(u)\big]dx \\ \displaystyle +\lambda \int_{\partial\Omega} \theta \cdot n\, ds \\ \displaystyle +r\left(\int_\Omega dx - V_{tar}\right)\int_{\partial\Omega} \theta \cdot n\, ds, \end{cases} \tag{27}$$

while for the displacement case, it takes the form

$$J'(u(\Omega))(\theta) = \begin{cases} \displaystyle\int_D \frac{\partial d_\Omega}{\partial \Omega}(\theta)\big[A'(d_\Omega)\,(e(u) - \alpha(d_\Omega)\Delta T)\, e(p) \\ -A(d_\Omega)\alpha'(d_\Omega)\Delta T e(p)\big]dx \\ \displaystyle +\lambda \int_{\partial\Omega} \theta \cdot n\, ds \\ \displaystyle +r\left(\int_\Omega dx - V_{tar}\right)\int_{\partial\Omega} \theta \cdot n\, ds. \end{cases} \tag{28}$$

The shape derivative of the signed-distance function has been discussed in detail in Allaire et al. (2014). The Eulerian derivative of d_Ω was found to be

$$\frac{\partial d_\Omega}{\partial \Omega}(\theta)(x) = -\theta(p_{\partial\Omega}(x)) \cdot n(p_{\partial\Omega}(x)) \quad \text{for any point } x \in D, \tag{29}$$

where $p_{\partial\Omega}(x)$ denotes the orthogonal projection of x on the boundary of Ω.

Substituting (29) in (27) and (28) does not directly provide an explicit descent direction, i.e., a vector field, θ, along which the interface $\partial\Omega$ should be moved. Instead, a coarea formula is used to obtain the standard form of the shape derivative (Allaire et al. 2014):

$$J'(u(\Omega))(\theta) = \int_{\partial\Omega} \theta(s) \cdot n(s)\; j'(\Omega)(s) ds, \tag{30}$$

which gives a descent direction using $\theta(s) = -j'(\Omega)(s)\, n(s)$.

This form of the shape derivative provides a descent direction only on the interface $\partial\Omega$, which is limiting from a numerical point of view. Therefore, an additional step is added to extend and regularize the shape derivative to the whole working domain D (see Allaire et al. 2004, 2014). The shape transformation occurs through the transport of a level set function via a Hamilton-Jacobi equation (Allaire et al. 2004).

A corresponding optimization algorithm has been implemented in Scilab (Version 5.3.3) (Scilab Enterprises 2012), a software for numerical computation, and is as follows:

Algorithm for 2D shape optimization under an area equality constraint.

1. Initialize the level set function to obtain a starting geometry and area fraction.
2. While the maximum number of iterations is not reached:
   (a) Evaluate the objective function and shape derivative.
   (b) Deform the shape by transporting the level set function with the Hamilton-Jacobi equation. The equation is solved on a time step dt and for a normal velocity $V = -j'(\Omega)$.
   (c) Update the Lagrange coefficient based on its previous value and the previous constraint errors.
   (d) Reinitialize the level set function to the signed distance function. This improves the conditioning for the Hamilton-Jacobi equation while keeping the same zero contour or level line.

3 Results of numerical examples

In this section, several examples of topology optimization with two isotropic materials A, B (Fig. 3) or two materials and void are presented. They illustrate the benefits of optimization schemes that account for features at the interfacial level that are either by design or unavoidable and

are derived from the fabrication and manufacturing processes when multiple materials are involved. The objective or cost functional is, in the first examples, the minimization of the compliance or work done by the loads. Elastic structures comprised of two materials are presented, followed by elastic structures with two materials and void. Finally, a two-material thermoelastic case is also discussed.

In order to better visualize trends for the bi-material cases, equality constraints on the lower modulus or higher CTE bulk material are imposed (50 % of the domain). Note that this constraint is not necessarily arbitrary. It can, for example, be beneficial when use of a less expensive material with inferior properties is desired. Additional constraints that are specific to individual manufacturing processes are not included in this initial 2D study. Further work in 3D could include for example, constraints based on thermal stress induced warping that occurs in some types of 3D printing processes.

In all of the strictly two material cases, unless otherwise noted, the following parameters were used in obtaining the results. Poisson's ratio was kept constant at 0.3. The applied point-load force was normalized to unity ($g = 1$) and a normalized Young's modulus $E_A = 1$ was used. These normalized parameters were used without loss of generality because the problem is within the domain of linear elasticity. Moreover, these non-dimensional properties remain representative for a variety of engineering applications. The inelastic strain ($\alpha \Delta T$), resulted from a distributed load provided by a uniform thermal excursion (ΔT). Although the inelastic strain is presented as originating from thermal expansion, it is also analogous to swelling in problems of soft materials like some polymers or biological materials. Thus interpretation of the thermoelastic results below is not restricted to thermal effects.

Two loading conditions were considered. The first kind of problem was purely mechanical with a point-load force (no thermal excursion) (Figs. 5 and 10). The second kind of problem involved only distributed or bulk force loading via a uniform thermal excursion (Fig. 14, $\Delta T = 1$). These numerical tests with point loads or uniform bulk force loading were chosen in order to comply with the usual benchmark problems (Rozvany 1998; Bulman et al. 2001; Allaire et al. 2004; Challis 2010; Wang and Wang 2004; Xia and Wang 2008b). However considering more realistic distributed loads is no more difficult than point loads (Allaire et al. 2004; Sigmund and Clausen 2007), but will be the topic of future work for more specialized applications. For compliance minimization problems it is commonly accepted that, in numerical practice, the application of point loads yields the same optimal shapes as distributed loads (this does not hold true for stress-based objective functions).

Typically, at least 400 optimization iterations were performed to ensure convergence in the optimization process. For the cases shown in Figs. 5 and 14, symmetry was employed such that only one-half of the numerical domain was needed. A variety of mesh densities were investigated for the finite element analysis and results are presented with a fine mesh (150 elements in the x_1-direction and 150 elements in the x_2-direction, Fig. 5). This mesh choice is also informed by mesh sensitivity studies performed elsewhere (Allaire et al. 2014). The magnitude of the interface zone thickness has been kept constant by setting $\epsilon = 4dx$, where ϵ is half of the total interface zone thickness and dx is the element size (Fig. 3).

Most cases in the following sections were initialized with inclusions of material B distributed within a matrix of material A. This choice of initialization is typical for topology optimization by the level set method because there is usually no independent material nucleation mechanism included in the algorithm (Section 2.1.2). Nevertheless, the present algorithm is still capable of topology optimization: inclusions may still pinch off, merge, or morph, to create topological changes in 2D (Allaire et al. 2004).

3.1 Using monotonically graded interfaces

The Young's modulus, E, and CTE, α, were smoothly interpolated (C-1 continuous) between bulk values: E_A and E_B; α_A and α_B. For example, in the case of the Young's Modulus, the variation of E across an interface was prescribed by:

$$E = E_A + h_{int}^{mono}(E_B - E_A). \tag{31}$$

The monotonic interpolation scheme, h_{int}^{mono}, used was that proposed by Osher and Fedkiw (2002):

$$h_{int}^{mono} = \begin{cases} 0, & \text{if } d_\Omega < -\epsilon \\ \frac{1}{2} + \frac{d_\Omega}{2\epsilon} + \frac{1}{2\pi} sin\frac{\pi d_\Omega}{\epsilon}, & \text{if } \mid d_\Omega \mid < \epsilon \\ 1, & \text{if } d_\Omega > \epsilon, \end{cases} \tag{32}$$

where the signed-distance function, d_Ω, was used for the interpolation instead of the level set function, ϕ, The level set function ϕ still describes and advects the shape.

3.2 Using non-monotonically graded interfaces

For non-monotonic interface interpolation, a 6th-order polynomial was employed whose coefficients were determined by imposed constraints. At the borders of the interface zone ($d_\Omega = \pm\varepsilon$), the bulk material properties must be recovered, i.e. E_A or E_B, α_A or α_B. Moreover, the material property distributions must be C-1 continuous, so that the first derivatives at the interface zone boundaries ($d_\Omega = \pm\varepsilon$, Fig. 3), were also required to be zero. Two coefficients and two boundary conditions remain. As the interpolation

is non-monotonic, the presence of an intermediate maximum or minimum in the interpolation function is assumed. Presently, the location of this maximum or minimum is fixed to be at $d_\Omega = 0$, Fig. 3. It is worth noting that this non-monotonically graded interface interpolation scheme would not be tractable using previous formulations of the shape derivative because those previous formulations depend only on the value of the interpolation derivative at $d_\Omega = 0$, which is zero in this case.

For an intermediate maximum at $d_\Omega = 0$, the property value, P, is $P_{d_\Omega=0} = mval * (max(P_A, P_B))$ and similarly for an intermediate minimum at $d_\Omega = 0$, the property value, P, is $P_{d_\Omega=0} = mval * (min(P_A, P_B))$. Where $mval$ is the multiplying factor that determines the nature of the interface zone transition between the bulk properties P_A and P_B (Fig. 3). The final coefficient is solved for by requiring that the first derivative at the location of the intermediate maximum or minimum is also zero. For example, in the case of the Young's Modulus ($P = E$), the variation of E across the interfacial interpolation zone, between the bulk values of E_A, E_B, was:

$$E = h_0 + E_A h_1 + E_B h_2, \tag{33}$$

where

$$h_0 = \begin{cases} 0, & \text{if} \quad d_\Omega \quad < -\varepsilon \\ mval - d_\Omega^2 \left(\frac{2\,mval}{\varepsilon^2} - \frac{mval\, d_\Omega^2}{\varepsilon^4} \right), & \text{if} \mid d_\Omega \mid < \varepsilon \\ 0, & \text{if} \quad d_\Omega \quad > \varepsilon \end{cases} \tag{34}$$

and

$$h_1 = \begin{cases} 1, & \text{if} \quad d_\Omega \quad < -\varepsilon \\ -d_\Omega^2 \left(d_\Omega (\frac{5}{4\varepsilon^3} - d_\Omega (\frac{3d_\Omega}{4\varepsilon^5} - \frac{1}{2\varepsilon^4})) - \frac{1}{\varepsilon^2} \right), & \text{if} \mid d_\Omega \mid < \varepsilon \\ 0, & \text{if} \quad d_\Omega \quad > \varepsilon \end{cases} \tag{35}$$

and

$$h_2 = \begin{cases} 0, & \text{if} \quad d_\Omega \quad < -\varepsilon \\ d_\Omega^2 \left(d_\Omega (\frac{5}{4\varepsilon^3} - d_\Omega (\frac{3d_\Omega}{4\varepsilon^5} + \frac{1}{2\varepsilon^4})) + \frac{1}{\varepsilon^2} \right), & \text{if} \mid d_\Omega \mid < \varepsilon \\ 1, & \text{if} \quad d_\Omega \quad > \varepsilon. \end{cases} \tag{36}$$

By taking account of material interface characteristics, the number of potential design parameters has significantly increased to include the thickness of the interfacial zone and six possible profiles for each of the properties E and CTE. These include: monotonically decreasing or increasing cases, and non-monotonically decreasing or increasing with an intermediate global maximum or minimum in the property values. In purely mechanical analyses, some of these aforementioned cases are redundant, but for thermoelastic analyses they remain relevant. Intermediate maximums or minimums that fall within the bounding values of the bulk properties are not of interest in this study.

However, not all of the possible combinations of monotonic and non-monotonic transition functions are physical, nor are they strictly independent. For example, typically, natural and man-made materials follow an anti-correlated relationship between Young's modulus and CTE due to interatomic energy considerations. Consequently, a material with high Young's modulus usually has lower values of CTE (Fig. 4 and see also for example, CES EduPack (Limited GD 2010)). Positively correlated relationships do exist, but are much more restrictive and are not considered herein. The thickness of the interfacial zone is also not strictly independent of the material choices, but it is treated as such for the purposes of this study due to the highly tunable nature of this parameter using heat treatments and innovative processing techniques.

3.2.1 Two-material elastic structure

The first example is a structure with a domain ratio of 2:1 that is fully clamped at both the right and left edges while being loaded vertically ($g = -1$) at the mid-point of the bottom edge (Fig. 5). The normalized domain size parameters are thus $h = 1$ and $w = 2$. This structure remains uniformly at its reference temperature, such that the thermoelastic formulation simplifies to the classic mechanical-only compliance problem. Two materials (A-blue, B-yellow) are assumed with a ratio of 10:1 for the Young's modulus (material A has a higher E). The problem includes an equality volume constraint ($V_{tar} = 0.5|D|$) on the lower modulus material-B using an augmented Lagrangian formulation. The half-domain is discretized on a fixed Eulerian grid with 150×150 quadrilateral elements (employing symmetry).

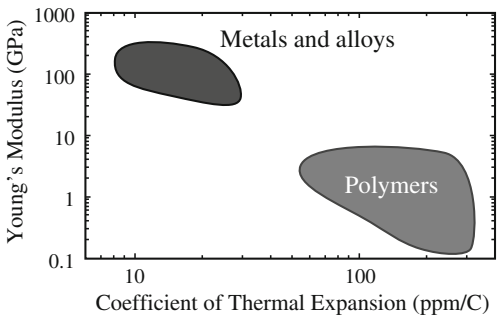

Fig. 4 Schematic plot of families of materials in the space of thermal expansion and stiffness

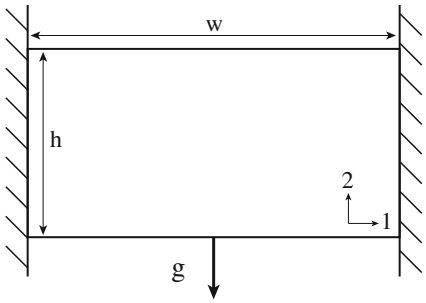

Fig. 5 The design problem for the built-in-beam with loading and boundary conditions

Analyses with two different property profiles were conducted. In the first case Fig. 6a, a monotonic transition across the graded material interface is used. This case was initialized with inclusions of material B distributed within a matrix of material A as shown in Fig. 6c, "Iteration 1." Fig. 6c also displays some intermediate results during the optimization interations and the final design on the full domain is shown in Fig. 6b.

In the second case, a non-monotonic transition was used that included an intermediate maximum such that the interface Young's modulus at $d_\Omega = 0$ Figs. 3, and 7a was two times greater than the larger bulk material modulus. This case was initialized (see Fig. 7c, "Iteration 1") using the solution from the previous monotonic result (Fig. 6b). Initializing from the previous final design, the properties within the interface width are reinterpreted using the non-monotonic scheme and the level set based optimization is able to improve upon the design, lowering the objective function (Table 1, see equation (14)).

Initializing the optimization with the previous solution allows direct comparison of the results, but can also be a restriction on the optimization as currently, the topological derivative is not included in the analysis. Without the topological derivative, nucleation of material A or B, is not possible. Nevertheless, significant topological changes can be made through the possibility of merging. As such, a third example (Fig. 8) with the same non-monotonic transition scheme is presented (Fig. 8a). The third example returns to the initialization scheme used in Fig. 6c and follows the same approach. The final design (Fig. 8b) is significantly different from the previous result in Fig. 7b.

To illustrate the design's further dependence on the interface property profile choice, a non-monotonic transition with a larger magnitude in its variation is introduced in Fig. 9. In this case, the non-monotonic transition includes an intermediate maximum such that the interface Young's modulus at $d_\Omega = 0$ is five times greater than the larger bulk material modulus, Fig. 9a. All four results are compared in Table 1. Table 1 also shows the objective and volume constraint convergence histories for each case. These histories illustrate the reductions in compliance attributed to the changing shape and topology while showing how closely the volume constraint is respected. All of the non-monotonic schemes improve on the objective function defined as the minimization of the compliance of the structure. The more non-monotone the interface is, the more complex is the

Fig. 6 Case for monotonic interface interpolation applied in the built-in-beam subjected to a point load (Fig. 5). Results shown on the half-domain unless otherwise noted. The design images show the distribution of materials A (*blue*) and B (*yellow*) in the domain, with the interface zone highlighted in *red*

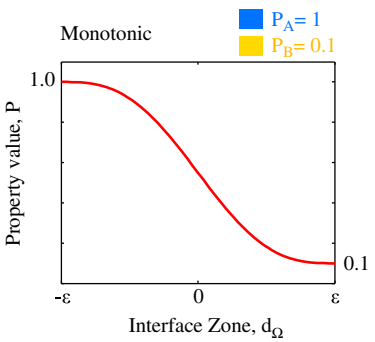

(a) Young's Modulus.

(b) Final design on the full-domain.

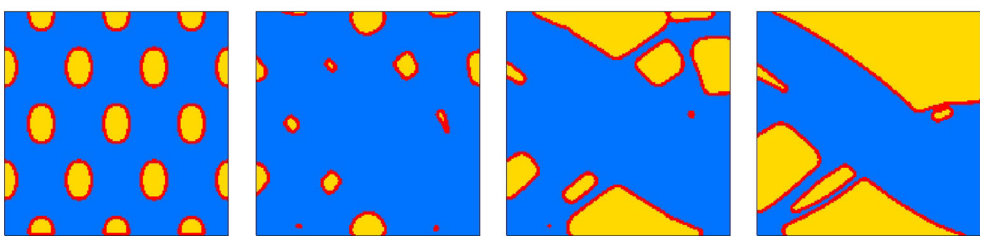

(c) Iterations 1, 10, 25, 40.

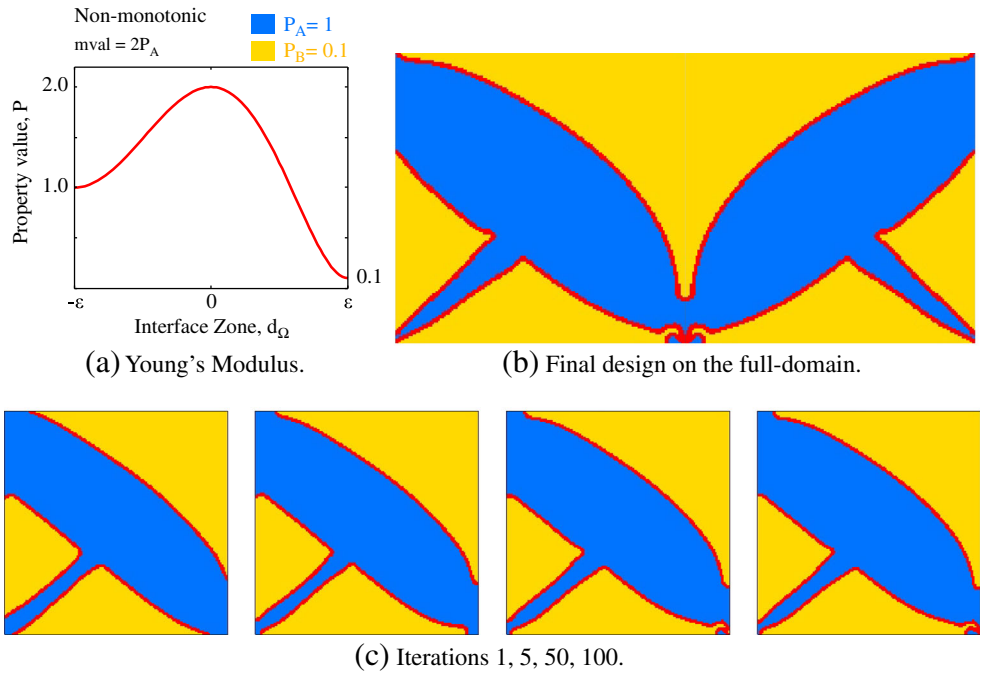

(a) Young's Modulus. (b) Final design on the full-domain.

(c) Iterations 1, 5, 50, 100.

Fig. 7 Case for non-monotonic interface interpolation applied in the built-in-beam problem (Fig. 5). Results were initialized ("Iteration 1" in (**c**)) with the final design from the monotonic interface interpolation scheme (see Fig. 6(b))

optimal topology since the interface zone has a higher Young's modulus than either of the bulk materials. Initializing from the monotonic solution yields a 29 % reduction and initializing with the same inclusion scheme as the monotonic-transition case yields a 35 % reduction in the structural compliance. Enhancing the interface property disparity even further ($5 \times max\,(E_A, E_B)$) yields a 69 % reduction in the objective compliance.

3.2.2 Elastic structure with two materials and void

Next, the classic short-cantilever problem (Wang and Wang 2004) of compliance minimization that yields a two-bar frame is considered (Fig. 10). The design domain consists of a rectangular area with the normalized size parameters $h = 1$ and $w = 2$. A normalized vertical load of value $g = -1$ is applied at the middle of the right edge and the boundary is fixed ($u_1 = u_2 = 0$) on the left edge. There is no thermal load applied to this structure so that comparison with the classic analytical optimum-topology solution of two beams at an angle of 45° that supports the applied load can be made. The two materials assumed have a ratio of 2:1 for the Young's modulus and the same Poisson's ratio (ν =0.3). The problem includes equality constraints on the volume of each of the materials using an augmented Lagrangian formulation. The volume constraints are 10 and 20 % of the domain for the higher and lower modulus materials, respectively, as was done in Wang and Wang (2004). The full design domain is discretized on a fixed Eulerian grid with 80 × 160 quadrilateral elements.

Two level set functions are employed. Their combination can describe up to four distinct phases. In this case, the level sets represent two material phases: material A (higher E_A) and material B (lower E_B), and two phases of void. The external interfaces between material and void are treated with a fixed width; the same width is enforced between the internal material interfaces ($\varepsilon = 2dx$). This width is considered "thin" or "sharp" in comparison with the thicker material interface results presented in Section 3.2.1, in order to correspond more closely with the work presented in Wang and Wang (2004). The phases representing void are modeled using the traditional ersatz material approach with an extremely weak normalized Young's modulus ($E_{void} = 0.001$).

Analyses with two different property profiles were conducted (Figs. 11–13). In all cases contours of the Young's modulus are shown in greyscale in the results. In the first case, a monotonic transition across the "sharp" material interface is employed, Fig. 11a. This case was initialized with distributed voids or pores in the initial design as shown in Fig. 11c "Iteration 1", with the rest of the domain consisting of the first and second materials. Figure 11c also displays some intermediate results during the optimization and the final design is shown in Fig. 11b.

In the second case (Fig. 12), a non-monotonic transition was used that included an intermediate maximum such that the interface Young's modulus at $d_\Omega = 0$ was two times greater than the larger bulk material modulus, Fig. 12a. This case was initialized (Fig. 12c, "Iteration 1") using the solu-

Table 1 A table of final objective function values for the minimization of the compliance of the built-in beam problem (Fig. 5) for different property transition profiles

Case	Objective convergence	Volume convergence	Final objective
Figure 6	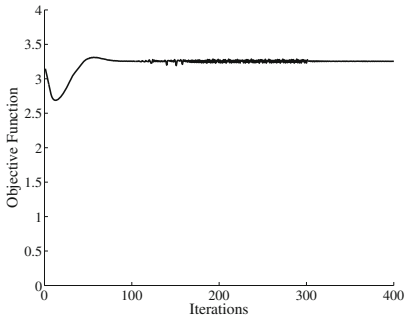	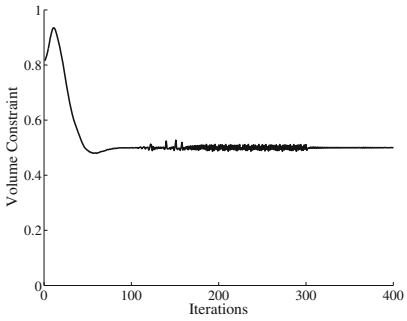	3.25
Figure 7	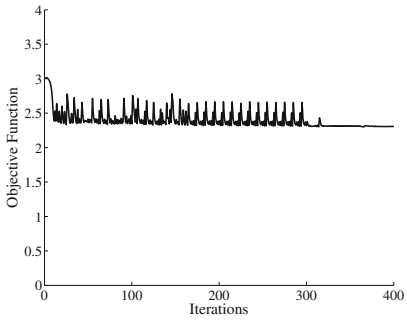	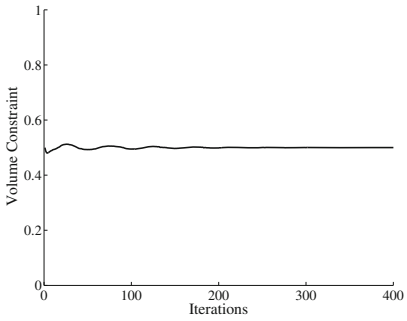	2.30
Figure 8	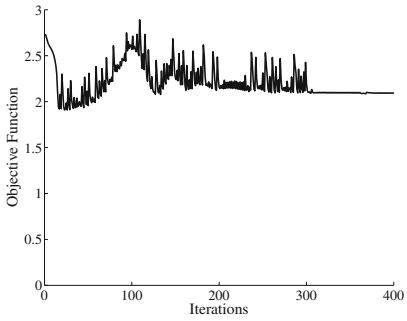	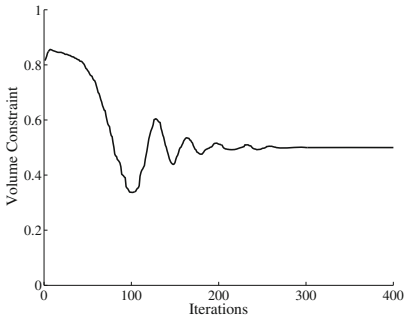	2.10
Figure 9	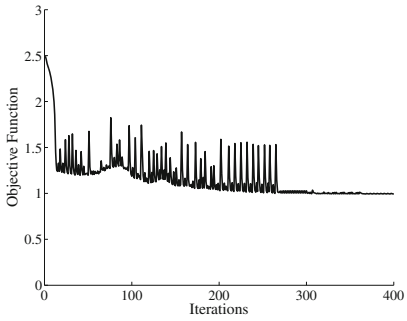	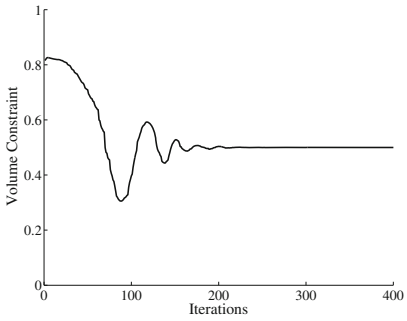	1.00

All results used $\varepsilon = 4dx$ (Fig. 3) and a 150 × 150 element mesh on the half-domain

tion from the previous monotonic result (Fig. 11b). Using this initialization, the properties within the interface width are reinterpreted using the non-monotonic scheme and the level set based optimization is able to improve upon the design, lowering the objective compliance function (Table 2, see equation (14)).

As before, initializing the optimization with the previous solution can be a restriction on the optimization and a third example (Fig. 13) is presented. This example has the same non-monotonic transition scheme, Fig. 13a, as Fig. 12a. The example in Fig. 13, returns to the initialization scheme used in Fig. 11c and follows the same approach. All

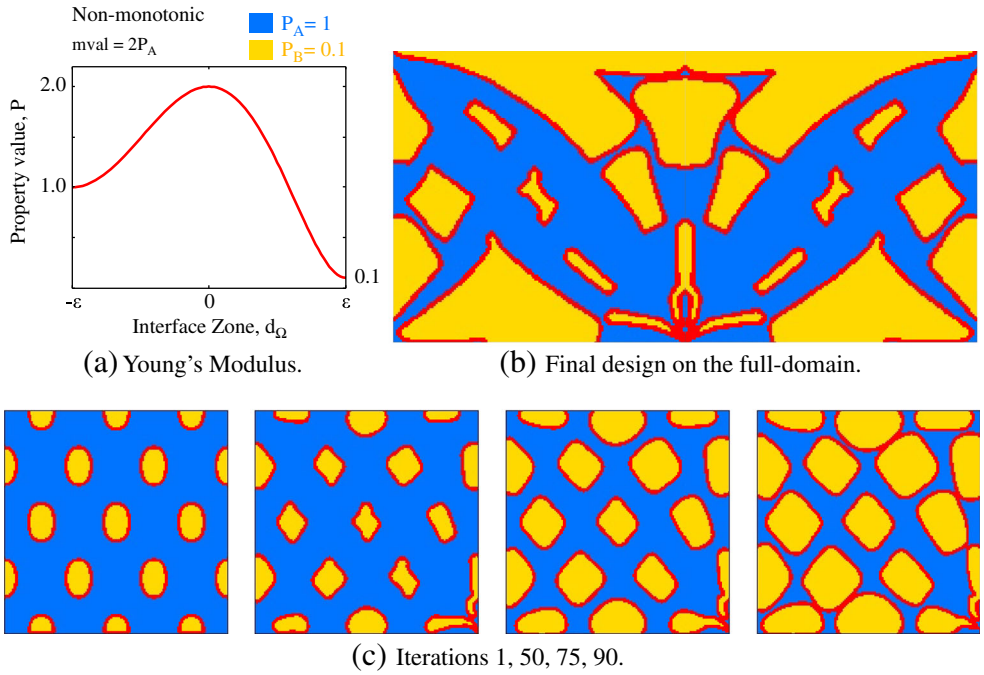

(a) Young's Modulus. (b) Final design on the full-domain.

(c) Iterations 1, 50, 75, 90.

Fig. 8 Case for non-monotonic interface interpolation applied in the built-in-beam problem (Fig. 5). Results were initialized from a regular array of inclusions ("Iteration 1" in (**c**)) and are shown on the half-domain unless otherwise noted

three results are compared in Table 2 where it is seen that both of the non-monotonic schemes improve on the objective function: initializing from the monotonic solution yields a 24 % reduction and intializing with the same shape as the monotonic design yields a 28 % reduction in the objective compliance function. Table 2 also presents the objective function and volume constraint on material-A convergence histories for each case. The volume constraint on material-B has similar convergence and is not shown.

3.2.3 Two materials in a thermoelastic structure

As previously in Section 3.2.1, the built-in beam with two materials and without void is chosen as the configuration for study. This problem is related to that studied in Xia and Wang (2008b). A normalized and uniform Young's modulus $E_A = E_B = 1$ is used. The contrast in CTE is $\alpha_A/\alpha_B = 2/3$, where α_A and α_B are proportional to the identity tensor. A uniform thermal excursion of $\Delta T = 1$

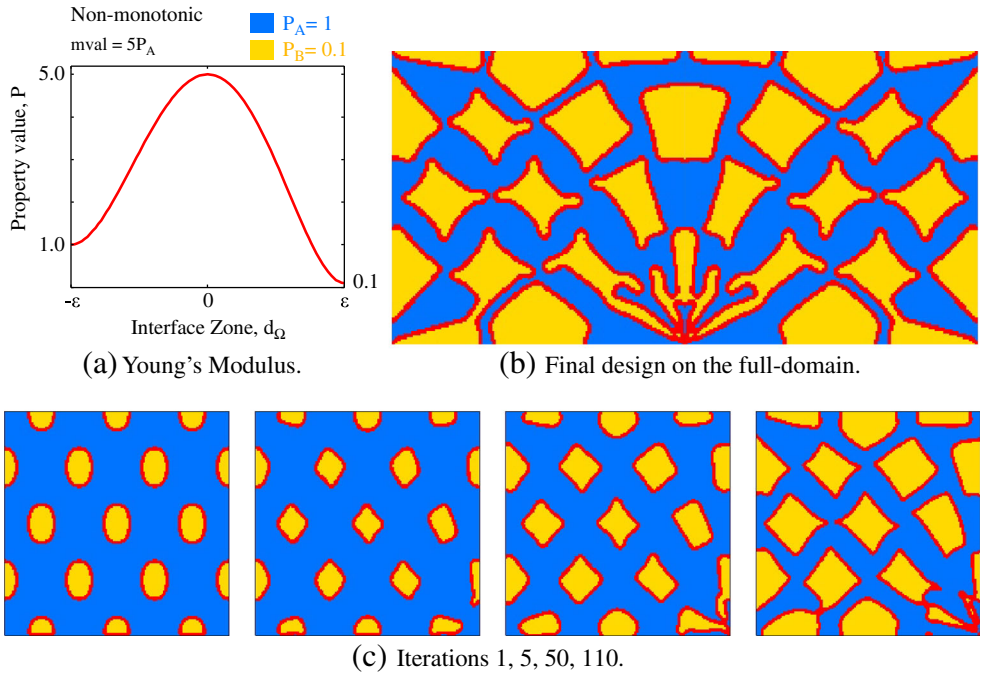

(a) Young's Modulus. (b) Final design on the full-domain.

(c) Iterations 1, 5, 50, 110.

Fig. 9 Case for another non-monotonic interface interpolation scheme applied in the built-in-beam problem. Results were initialized from a regular array of inclusions ("Iteration 1" in (**c**)) and are shown on the half-domain unless otherwise noted

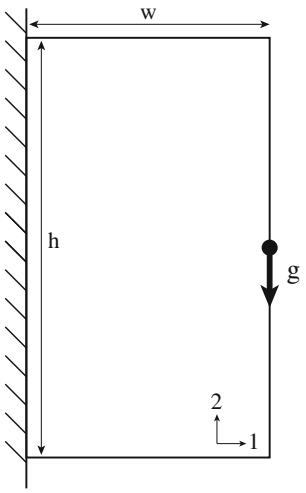

Fig. 10 The mechanical design problem for the short-cantilever with loading and boundary conditions

is imposed (Fig. 14) and the objective function is altered to minimize the square of the displacement (x_2-direction) at the point of interest in Fig. 14 (see equation (21)). The normalized domain size parameters are again $h = 1$ and $w = 2$. The volume constraint on the larger CTE material-B is 50 % of the domain. The other parameters are unchanged and the optimization results are shown in Figs. 15–18.

In the first case (Fig. 15), a monotonic interface transition is considered. The final design in Fig. 15c resembles a checkerboard pattern which may be intuitive as an arrangement of the materials that minimizes vertical displacement in Fig. 14. To check this intuition, a second case with monotonic property transition was also conducted and is shown in Fig. 16. This case was initialized with an idealized checkerboard pattern and it is seen that both the initialization from the regular array of inclusions and this case evolve towards a biased checkerboard final design (Figs. 15c, 16c).

In Fig. 17, the non-monotonic transition included an intermediate maximum in the CTE such that the interface CTE at $d_\Omega = 0$ was two times greater than the smaller bulk CTE and the Young's modulus remained uniform across the bi-material interface (Fig. 17a, b). This case was initialized (see "Iteration 1" in Fig. 16d) using the solution from the previous monotonic result (Fig. 15c).

In the last case, Fig. 18, the non-monotonic transition scheme from Fig. 17a, b is utilized. Figure 18 returns to the initialization scheme used in Fig. 15d and follows the same approach. All four results are compared in Table 3 where it is seen that only one of the non-monotonic results (rows 3 and 4) is able to improve on the final objective function values compared to the monotonic transition results (rows 1 and 2). When initializing from the monotonic solution, the monotonic final design is reinterpreted with the non-monotonic material properties and the resulting *initial* objective function value: the value at "Iteration 1", in row 3 of Table 3 is higher than the final objective value in row 1

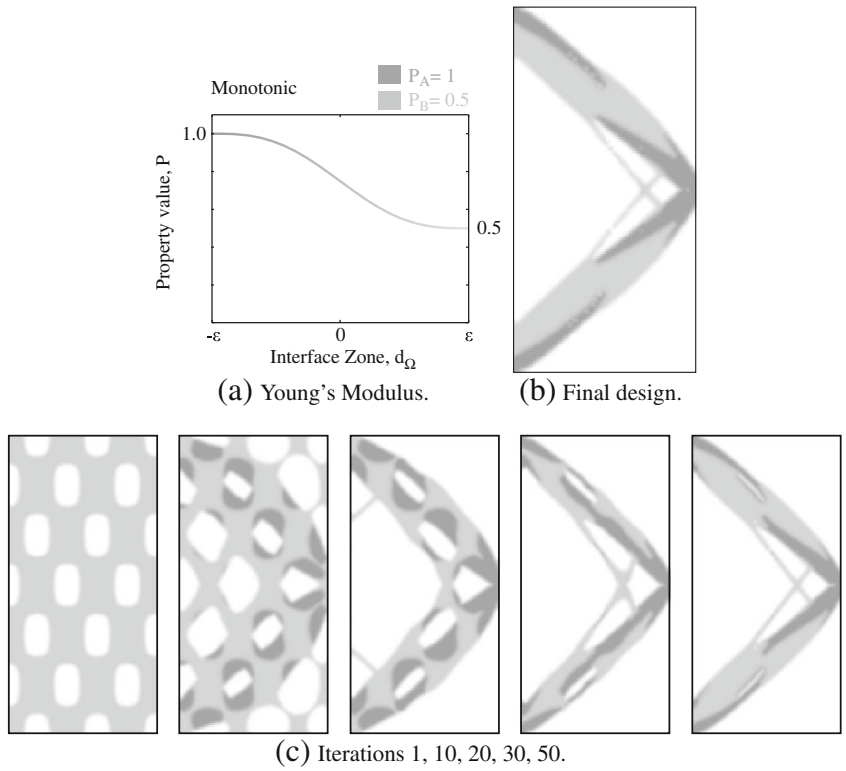

Fig. 11 Short-cantilever problem with two materials and void using monotonic interface interpolation. Results were initialized from a regular array of voids in the bulk materials. The design images show the distribution of Young's modulus in the domain: the higher modulus material (*medium grey*), lower modulus material (*light grey*) and void (*white*). With this scheme, the monotonic interface is not highlighted between the higher and lower modulus materials

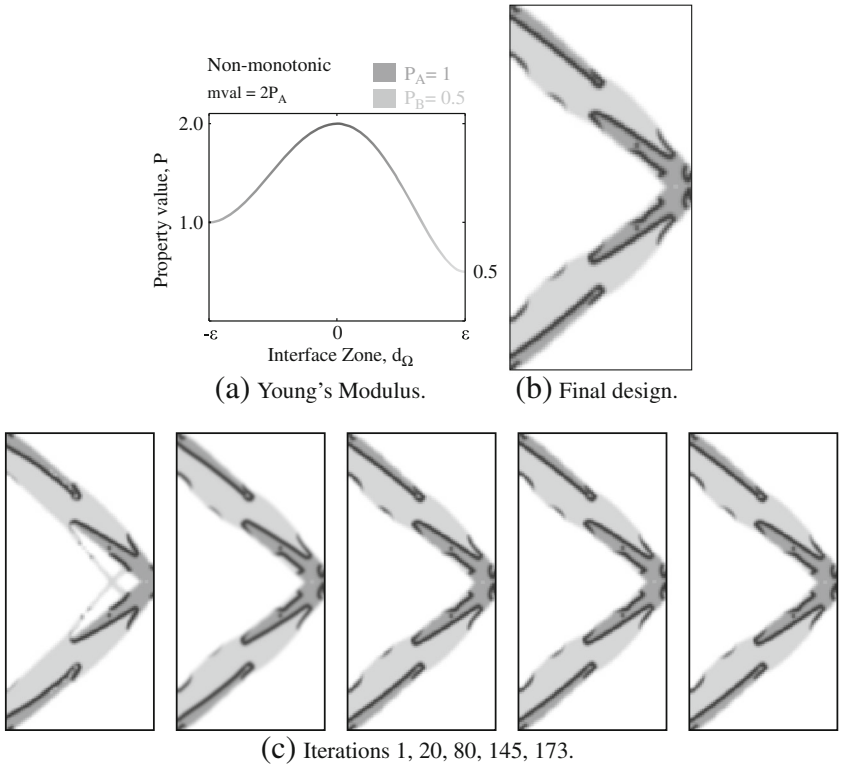

(a) Young's Modulus. (b) Final design.

(c) Iterations 1, 20, 80, 145, 173.

Fig. 12 Short-cantilever problem with two materials and void using non-monotonic interface interpolation. Results were initialized with the final design from the monotonic interface interpolation scheme (Fig. 11b). The design images show the distribution of Young's modulus in the domain: the higher modulus material (*medium grey*), lower modulus material (*light grey*) and void (*white*). With this scheme, the non-monotonic interface is highlighted in *dark grey* as it has the largest Young's modulus

of Table 3. As a result, although further iterations allow the objective function value to slightly decrease, the converged final design objective function value (last column in row 3 of Table 3 remains larger than the monotonic case's final objective function value (last column in row 1 of Table 3) by 6 %. When the non-monotonic initialization scheme uses

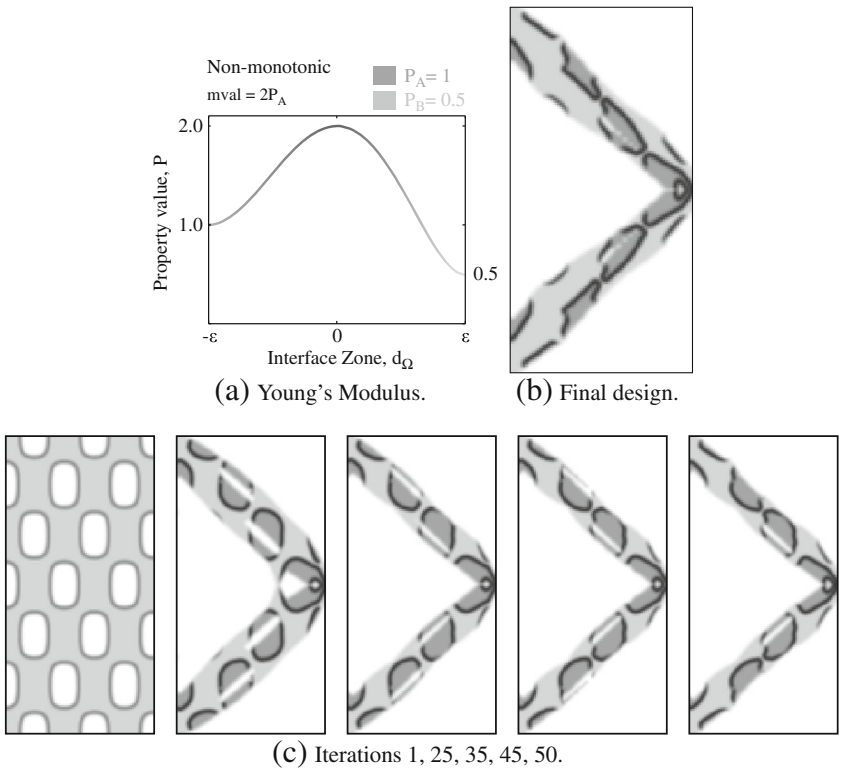

(a) Young's Modulus. (b) Final design.

(c) Iterations 1, 25, 35, 45, 50.

Fig. 13 Short-cantilever problem with two materials and void using non-monotonic interface interpolation. Results were initialized from a regular array of voids in the bulk materials. The design images show the distribution of Young's modulus in the domain: the higher modulus material (*medium grey*), lower modulus material (*light grey*) and void (*white*). With this scheme, the non-monotonic interface is highlighted in *dark grey* as it has the largest Young's modulus

Table 2 A table of final objective function values for the minimization of the compliance of the short-cantilever problem (Fig. 10) for different property transition profiles

Case	Objective convergence	Material A volume convergence	Final convergence
Figure 11	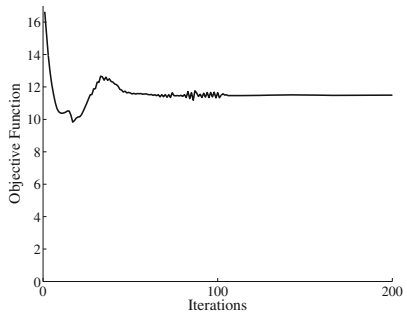	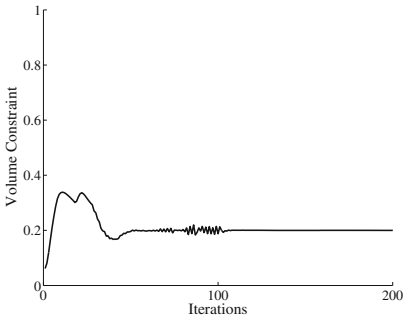	11.50
Figure 12	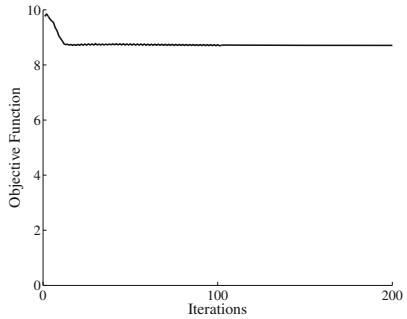	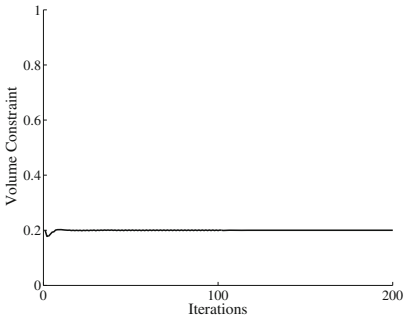	8.71
Figure 13	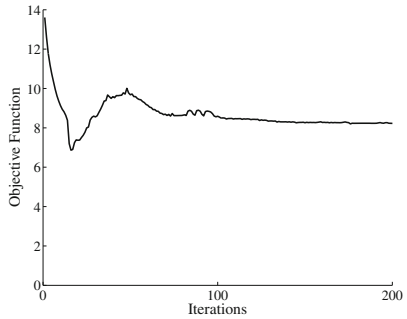	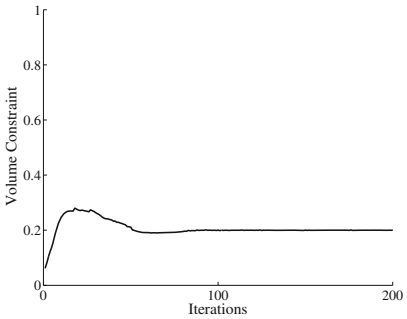	8.23

All results used $\varepsilon = 2dx$ (Fig. 3) and a 80 × 160 element mesh

the array of inclusions ("Iteration 1" in Fig. 18d), more topological changes are allowed and the non-monotonic solution is able to provide a 17 % decrease in the final objective function value, comparing rows 1 and 4.

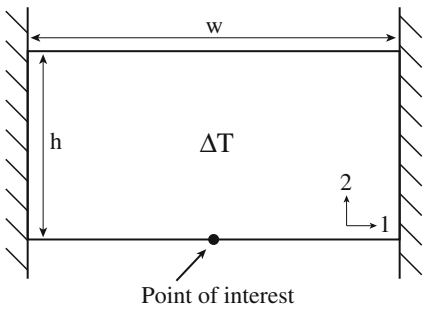

Fig. 14 The design problem for the built-in-beam with loading and boundary conditions. The analysis is thermoelastic with ΔT=1

4 Discussion

The interface between bulk materials is explicitly accounted for in the shape optimization problem outlined above via the level set method. In these first examples, isotropic bulk materials are considered, but extension to anisotropic properties or graded material regions as was done in Wang and Wang (2005) is also of interest. Several features related to the influence of the graded properties across the interface zone alone (Fig. 3) are highlighted below.

4.1 Sensitivity to interface interpolation scheme

As evidenced in the results above (Tables 1–3), the material interface zone interpolation scheme can significantly impact the efficacy of the design. Certainly for the elastic compliance and thermoelastic displacement problems investigated

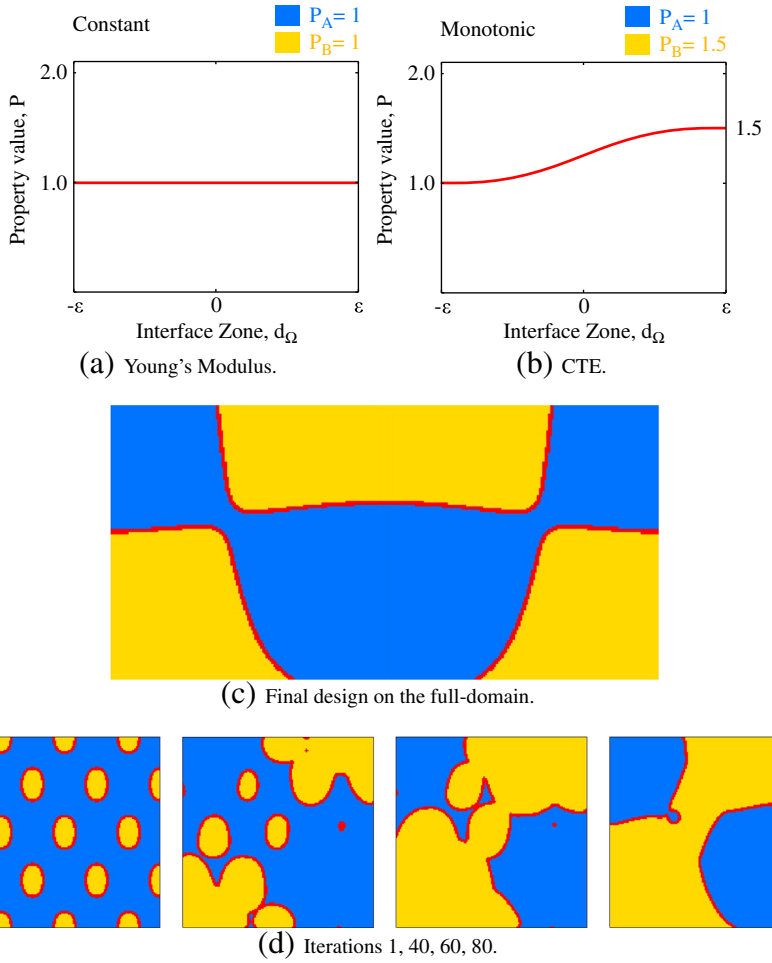

(a) Young's Modulus. (b) CTE.

(c) Final design on the full-domain.

(d) Iterations 1, 40, 60, 80.

Fig. 15 Case for monotonic interface interpolation applied in the built-in-beam problem under a thermal excursion (ΔT=1), Fig. 14. Results shown on the half-domain unless otherwise noted. The design images show the distribution of materials A (*blue*) and B (*yellow*) in the domain, with the interface zone highlighted in *red*

herein, the results are highly sensitive to initialization – as is commonly the case in optimization methods (Allaire et al. 2004). Sometimes, as in the case of one material and void problems of elastic compliance, a global optimum seems to be more easily established. Nevertheless, significant gains can be attained by taking more detailed account of interface characteristics in the optimization protocol. Alternatively, more conservative or realistic designs could also be found if the interface properties were considered deleterious in the design.

In the purely elastic compliance problems of Figs. 6 and 11, the monotonic treatment strongly resembles the classic one material and void result (Allaire et al. 2004; Wang and Wang 2004). This is to be expected because the lower modulus material simply replaces the void in the design. When non-monotonic transitions are employed that favor the interface (as the Young's modulus within the interfacial zone is twice that of the higher modulus material A), the optimal designs feature curved and sometimes tortuous interface trajectories that increase the interface perimeter while respecting the volume constraint. It should be noted that, in cases where the interface is clearly preferred (higher modulus in this problem), optimizing without the volume constraint produces designs in which the interface practically replaces the formerly strongest "bulk" material. As the interface thickness is fixed, designs in which one element of material A and material B are present only by definition, produce a worm-wood type structure that is neither physical nor illuminating, and are not presented herein.

In Fig. 7, the final design differs very little from the initialization. Recall this is the restrictive case as nucleation of material is not accounted for in the formulation of the problem. When initializing from the monotonic solution, small changes in the design (note the scale of the volume convergence diagrams in Table 1) cause significant reductions in the objective function and slightly curving the features compared to the monotonic design suffices to allow the optimization to converge to a local optimum and a 29 % compliance reduction (Table 1).

Initializing from the less restrictive array of inclusions in Fig. 8 allows a greater reduction in compliance with a significantly different final design. Cuboidal features with curved edges predominate. A slight resemblance to the monotonic final design (Fig. 6b) can still be found in that the higher

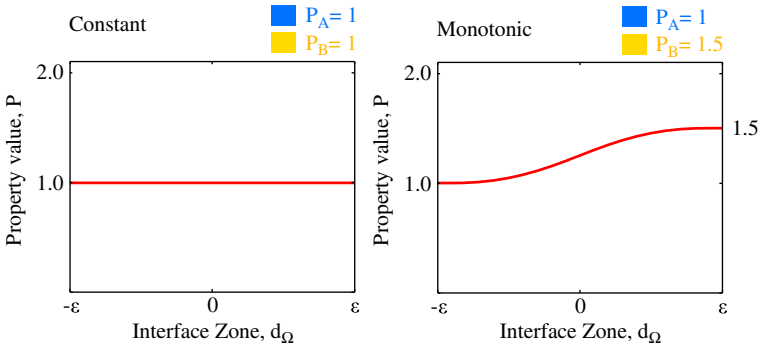

(a) Young's Modulus. (b) CTE.

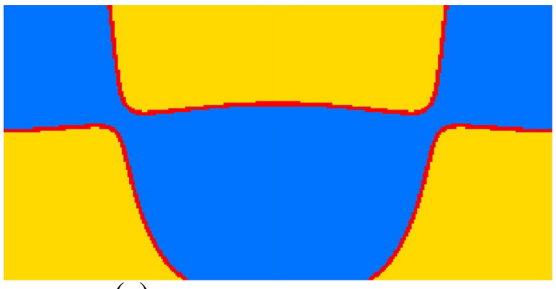

(c) Final design on the full-domain.

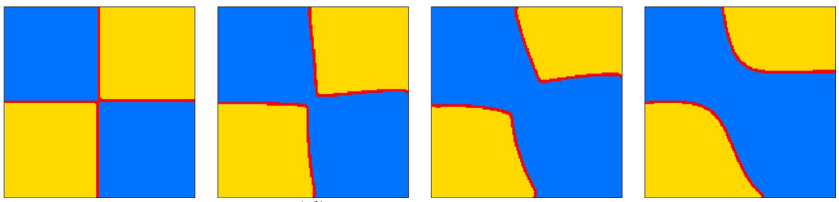

(d) Iterations 1, 10, 25, 40.

Fig. 16 Case for monotonic interface interpolation applied in the built-in-beam problem under a thermal excursion (ΔT=1), Fig. 14. Results shown on the half-domain unless otherwise noted. Results were initialized with the a checkerboard pattern ("Iteration 1" in (d)) inspired by the final design of the monotonic interface interpolation scheme (see Fig. 15c)

modulus material is present along the 45° line of force with a secondary support emanating from the bottom left corner at an angle of 45°. The smallest features are present at the point of loading which means that the interface is favored at this location.

By enhancing the favorable interfacial properties (Fig. 9), the propensity to promote curving trajectories that maximize the presence of the interface is revealed. Recall that the volume of the lower modulus material-B is always constrained to be 50 % of the design domain. In this case, a dog-bone-like structure is present, reminiscent of the theory of the equilibrium shape of crystals detailed by Wulff (Wulff 1901). Wulff's theory showed that the distance from a common center of a small crystallite to any given surface facet is proportional to the surface free energy of the facet. Here, surface free energy is not explicity included, but the interface stiffness properties being significantly higher than either of the bulk material moduli in a compliance minimization problem is a situation analogous to a theoretical crystallite transforming with low surface free energy. The optimal design follows a single orientation along the 45°line of force and the features comprised of material B (the lower modulus bulk material) remain of relatively uniform size, increasing the perimeter of the interface. Again the smallest features are found at the point of application of the load.

Similar trends are found in the case of the short-cantilever (Figs. 10–13). For ease of presentation, all results in these figures utilizing two materials and void show the distribution of Young's modulus in greyscale instead of the distribution of materials in color. The monotonic case, Fig. 11, results in the classic two-bar Michell-like structure (Michell 1904). The higher modulus material is more prevalent in the area where the load is applied (medium grey in Fig. 11b). When initializing from the monotonic solution, Fig. 12c "Iteration 1", minor changes in the design result in substantial decreases in the objective function value (Table 2), promoting little difference in the shape of the final design (Fig. 12b, c). The orientation of the beams is preserved and the interface with its favorable properties is

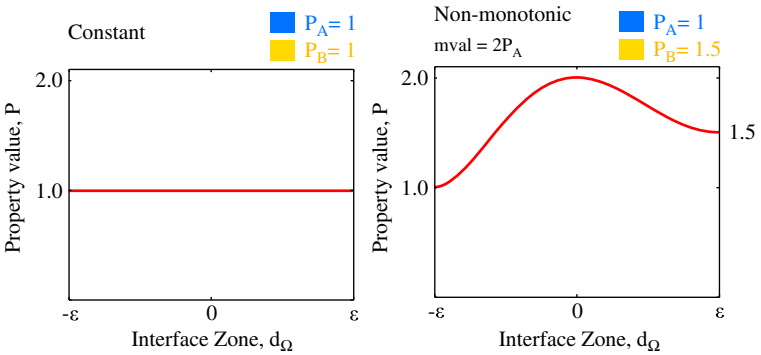

(a) Young's Modulus. (b) CTE.

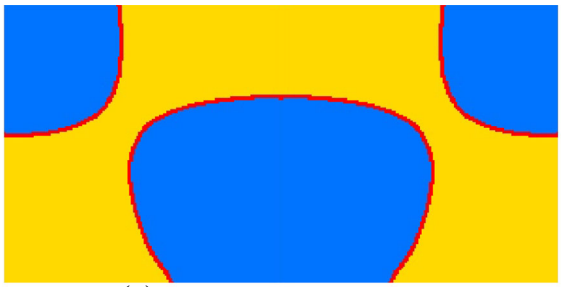

(c) Final design on the full-domain.

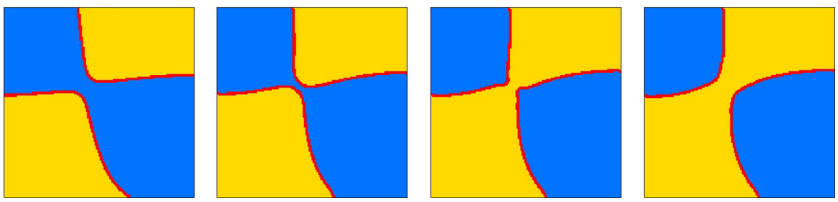

(d) Iterations 1, 20, 40, 80.

Fig. 17 Case for non-monotonic interface interpolation applied in the built-in-beam problem under a thermal excursion (ΔT=1), Fig. 14. Results shown on the half-domain unless otherwise noted. Results were initialized ("Iteration 1" in (**d**)) with the final design of the monotonic interface interpolation scheme (see Fig. 15c)

promoted towards the outer edges of the beams. In this final design (Fig. 12b), regions of the higher modulus material align such that sections of the interface line up along the 45° line of force and the interface perimeter is in general increased within the beams. The non-uniform beam thickness is promoted by the unequal volume constraints applied on the higher and lower modulus materials. By initializing from the array of voids (Fig. 13c) and enabling greater flexibility in favoring the interface, a more distributed design results that lowers the objective by 28 % (Table 2).

Finally, introducing the volumetric thermal loads in Figs. 14–18, introduces the opportunity for more complex conditions that are less intuitive. In order to start simply, the Young's modulus was assumed to be uniform for both materials and across the bi-material interface. A uniform thermal excursion $\Delta T = 1$ was imposed and the square of the displacement (x_2-direction) at the point of interest, displayed in Fig. 14, was minimized.

For the monotonic case, material A (blue) with the lowest CTE is clearly preferred at the point of interest where vertical displacement (in the x_2-direction in Fig. 14) is not desired. The final design, Fig. 15c, resembles a checkerboard arrangement of the two materials. The checkerboard pattern is an intuitive measure against vertical global displacement. However, the idealized checkerboard ("Iteration 1" in Fig. 16d), results in horizontal isocontours of displacement in the x_2-direction (Fig. 14). When the checkerboard pattern is slightly biased, as is seen in the final designs in Figs. 15c and 16c, the displacement at the point of interest is decreased.

The most effective design is found using the non-monotonic interface transition profile. When initializing from the monotonic solution (Fig. 17d "Iteration 1", see also Fig. 15c), no topological changes are made and very little benefit in decreasing the objective function value is derived (Table 3). However, when initializing from the array of inclusions (Fig. 18d "Iteration 1"), many topological changes occur that enable a 17 % reduction in the objective function value (comparing the last columns in rows 1 and 4 of Table 3). This is not intuitive as the interface has the largest CTE in the design domain. Instead of limited

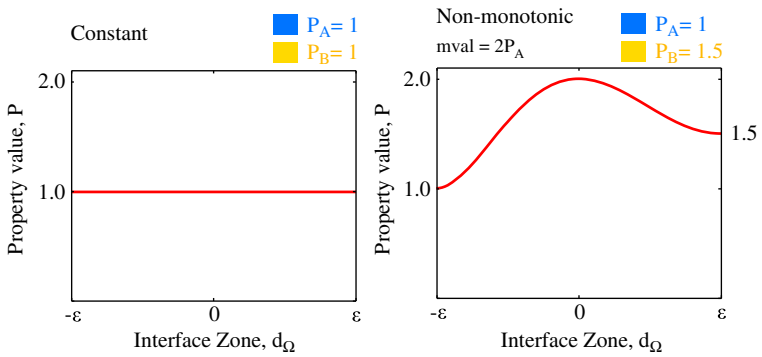

(a) Young's Modulus. (b) CTE.

(c) Final design on the full-domain.

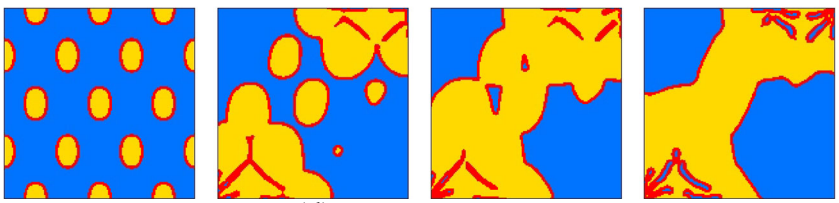

(d) Iterations 1, 45, 60, 90.

Fig. 18 Case for non-monotonic interface interpolation applied in the built-in-beam problem under a thermal excursion (ΔT=1), Fig. 14. Results were initialized from a regular array of inclusions ("Iteration 1" in (**d**)) and are shown on the half-domain unless otherwise noted

use of interfaces in the domain, the design features many oriented "fibers" of the interface at the corners and opposite the point of interest in Fig. 18c. While these interface "fibers" seemingly violate the assumption of the disparity of scales between the interface and the bulk materials, the results demonstrate the trend and more discussion on this point follows.

4.2 On the interface parameters

In contrast to previous level set topology optimization formulations, the interface zone width, ε (Fig. 3), is physically motivated and is not restricted to a convenient numerical approximation. Thus, the interface zone width introduces a length scale into the optimization problem. Nevertheless, final designs may be considered size-independent, provided everything, including the interface, is scaled uniformly.

However, changing only the interface zone width in the optimization formulation can affect the final optimized designs. Its influence is generally negligible when the dimensions of the optimized structure are much larger than *epsilon* (see Figs. 6b, 15c, 16c, 17c). Its influence becomes more important when the interface zone width approaches the same magnitude as the "bulk" material features in the design (see Figs. 7b, 8b, 9b, 12b, and 13b near the application of the point load or see the corners in Fig. 18c). The magnitude of the interface zone thickness (Fig. 3) has been kept constant: the length of 8 elements ($\varepsilon = 4dx$) for Figs. 6–9 and 15–18, and the length of 4 elements ($\varepsilon = 2dx$) for Figs. 11–13.

The fact that the interface zone thickness is fixed is a numerical restriction. It is not yet possible to continuously vary the width of the interface zone within the same design for the level set optimization framework. This restriction can be partially circumvented by parametrically varying the the thickness value to explore its effects.

Nevertheless, the interface thickness must also be sufficiently large compared to element size in order to adequately capture the non-monotonic nature of the property variations. Recall that a polynomial dictates the values at the elemental nodes within the interface region; this provides

Table 3 A table of final objective function values for the minimization of the vertical (u_2) displacement at the point of interest indicated in the built-in beam problem (Fig. 14) for different property transition profiles

Case	Objective convergence	Volume convergence	Final obj. $(u_2)^2$
Figure 15	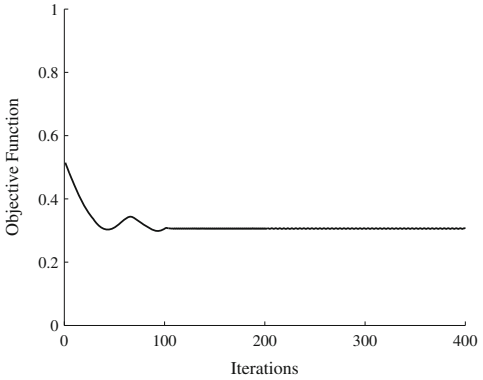	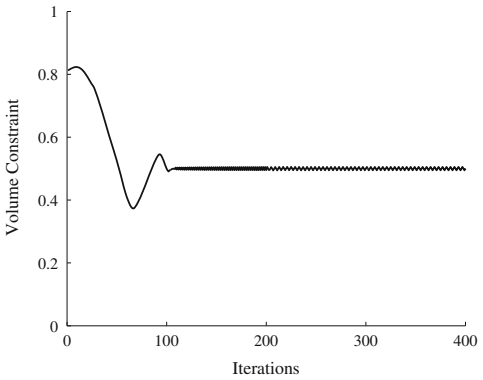	0.305
Figure 16	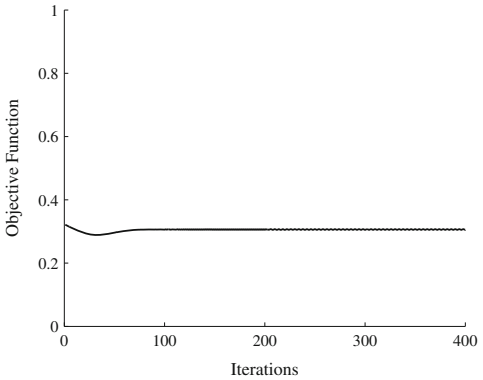	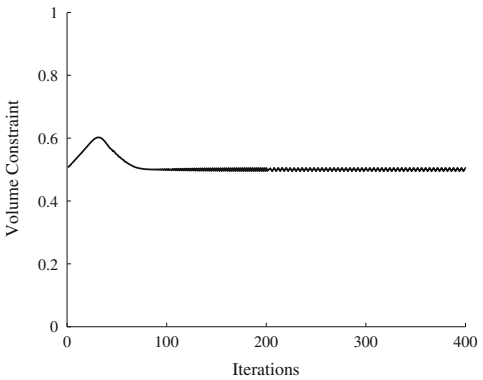	0.306
Figure 17	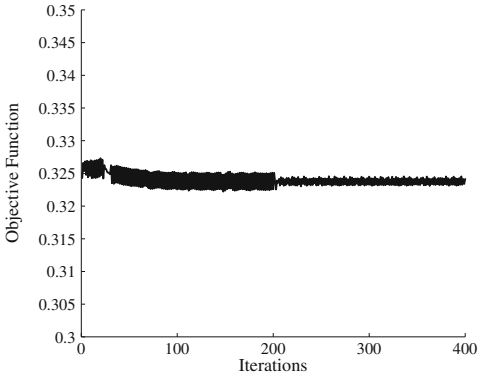	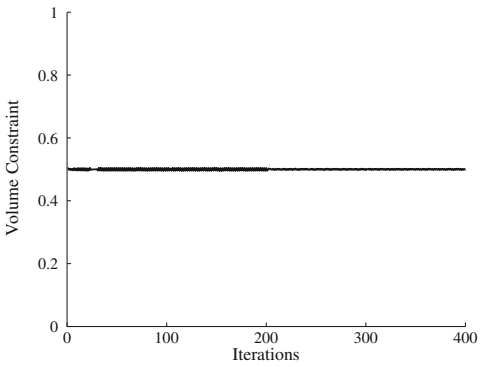	0.323
Figure 18	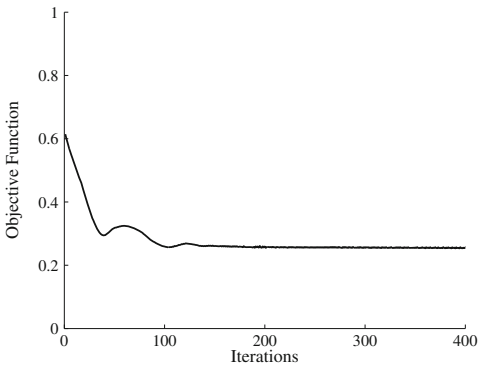	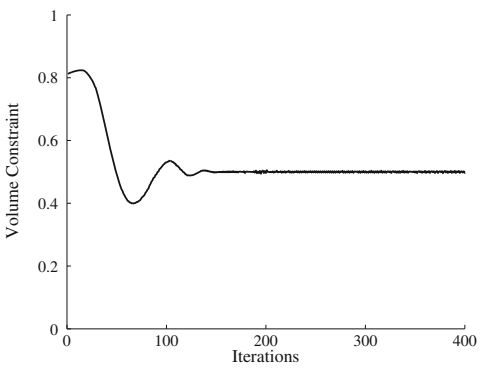	0.254

All results used a uniform normalized Young's modulus distribution ($E_A = E_B = E_{interface} = 1.0$), $\varepsilon = 4dx$, and a 150×150 element mesh on the half-domain

an estimate on the lower bound. At the other extreme, the interface region is typically energetically limited to approximately 10 % of the smallest feature of a design. As such, the interface does not saturate the design or become sandwiched between material features of comparable thickness to, or smaller thickness than, the interface zone. This final point, that all design features must remain at least 10 times greater in dimension than the fixed interface thickness, is a geometric constraint that is numerically difficult to directly implement. Indirectly, the requirement can be approximated by including interface perimeter penalization within the objective function. For the present work, neither approach is utilized and the unencumbered designs are presented to better illustrate the trends in interface effects. These trends may also be used to inspire more manufacturable manual interpretations of the final design as was done in Sigmund (2000). Accounting for *epsilon* as a length scale determines how refined the discretization needs to be and is likely to prevent mesh-dependencies in the optimization results. Moreover, we propose that future work decouples the definition of the interface interpolation zone width, ε, from the definition of the uniform grid mesh size. Instead, adaptive (non-uniform) mesh methods such as those found in Allaire et al. (2011) could be employed that would also allow a more detailed study of the influence of the interface zone thickness. Regardless of the meshing techniques, the fixed interface thickness distinguishes the effects of including interface characteristics from simply adding another bulk material. The interface is, by definition, sandwiched between materials A and B, whereas an additional bulk material, C, could be isolated within material A or B without contact to the remaining bulk material.

5 Conclusions

The influence of the interface between disparate bulk materials on the optimal design of elastic and thermoelastic structures has been investigated. The methodology employs a recent formulation that accounts for a finite interface zone in a shape optimization framework (Allaire et al. 2004). The description is extended to include a physically-motivated interface thickness with graded properties that can be monotonically varying between bulk materials but also non-monotonically varying with local properties that are larger or smaller than either of the bulk properties alone. Examples of these types of interface transitions, commonly found in materials science and biological materials, are given. The motivation of the present study is to highlight the importance of interface properties in optimal design and to direct the development of design tools that capitalize on advanced manufacturing capabilities. Two cases are presented: an elastic problem in which the compliance is minimized for a given point load and a thermoelastic case in which the displacement at a point of interest is minimized. An additional reference case, consisting in the minimization of the compliance of a short-cantilever beam, is also reported for comparison with similar shape optimization formulations found in Wang and Wang (2004). The main results are:

- Interface properties can be explicitly accounted for in shape optimization formulations. The interface thickness incorporates a physically motivated length scale into the problem formulation.
- The effect of interface properties depends both on the type of loading and boundary conditions of the problem considered, and on the transition profile relative to the bulk properties. The interface transition profiles identified are not restricted to an interval bounded by the surrounding bulk values but can be larger or smaller in magnitude.
- Accounting for interface properties can significantly improve the optimization results.
- The present formulation can be used to probe the influence of the interface characteristics in structures, but also to direct the development and processing of new materials, and in particular, bio-inspired materials. This is the aim of forthcoming studies.

Acknowledgements This work was supported by The Centre of Excellence of Multifunctional Architectured Materials sponsored by the French National Research Agency (LABEX CEMAM) and the French Ministry of Higher Education through the French University Institute (IUF) program. G. A. is a member of the Détermination de Formes et Identification (DEFI) project at INRIA Saclay Ile-de-France.

References

Allaire G, Bonnetier E, Francfort G, Jouve F (1997) Shape optimization by the homogenization method. Numerische Mathematik 76:27–68

Allaire G, Jouve F, Toader AM (2004) Structural optimization using sensitivity analysis and a level-set method. J Comput Phys 194:363–393

Allaire G, De Gournay F, Jouve F, Toader A (2005) Structural optimization using topological and shape sensitivity via a level set method. Control Cybern 34(1):59

Allaire G, Dapogny C, Frey P (2011) Topology and geometry optimization of elastic structures by exact deformation of simplicial mesh. Comptes Rendus Mathematique 349(17):999–1003

Allaire G, Dapogny C, Delgado G, Michailidis G (2014) Multi-phase structural optimization via a level set method. ESAIM: Control, Optimisation and Calculus of Variations, vol 20, pp 576–611. doi:10.1051/cocv/2013076

Bendsoe M, Kikuchi N (1988) Generating optimal topologies in structural design using a homogenization method. Comput Methods in Applied Mech Eng 71:197–224

Bendsoe M, Sigmund O (1999) Material interpolation schemes in topology optimization. Arch Appl Mech 69:635–654
Bendsoe M, Sigmund O (2004) Topology optimization: theory, methods and applications. Springer
Braccini M, Dupeux M (2012) Mechanics of solid interfaces. Wiley Online Library
Bulman S, Sienz J, Hinton E (2001) Comparisons between algorithms for structural topology optimization using a series of benchmark studies. Comput Struct 79(12):1203–1218
Céa J (1986) Conception optimale ou identification de formes: calcul rapide de la dérivée directionnelle de la fonction cout. Modélisation mathématique et analyse numérique 20:371–402
Challis VJ (2010) A discrete level-set topology optimization code written in matlab. Struct Multidiscip Optim 41(3):453–464
Committee on Integrated Computational Materials Engineering (2008) NRC Integrated computational materials engineering: a transformational discipline for improved competitiveness and national security. The National Academies Press. http://www.nap.edu/openbook.php?record_id=12199
Creton C, Kramer EJ, Brown HR, Hui CY (2002) Adhesion and fracture of interfaces between immiscible polymers: from the molecular to the continuum scale. In: Molecular simulation fracture gel theory. Springer, Berlin Heidelberg, pp 53–136
Eschenauer H, Olhoff N (2001) Topology optimization of continuum structures: a review. Appl Mech Rev 54(4):331–390
Guggenheim E (1959) Thermodynamics. North Holland Publishing Company
Harrysson OL, Cansizoglu O, Marcellin-Little DJ, Cormier DR, West IIHA (2008) Direct metal fabrication of titanium implants with tailored materials and mechanical properties using electron beam melting technology. Mater Sci Eng C 28(3):366–373
Ikuta K, Hirowatari K (1993) Real three dimensional micro fabrication using stereo lithography and metal molding. In: Micro electro mechanical systems, 1993, MEMS'93, proceedings an investigation of micro structures, sensors, actuators, machines and systems. IEEE, pp 42–47
Laszczyk L (2011) Homogenization and topological optimization of architectured panels. PhD thesis, Universite de Grenoble
Limited GD (2010)
Lipson H, Pollack JB (2000) Automatic design and manufacture of robotic lifeforms. Nature 406(6799):974–978
Mello LAM, Silva ECN (2013) Conceptual design of electorthermomechanical microactuators with functionally graded metallic materials using topology optimization for response time reduction. In: 10th World congress on structural and multidisciplinary optimization, May19-24, Orlando, Florida, USA
Michell AGM (1904) The limits of economy of material in frame-structures. Phil Mag 8:589–597
Miyamoto Y, Kaysser W, Rabin B, Kawasaki A, Ford R (1999) Functionally graded materials: design, processing and applications
Osher S, Fedkiw R (2002) Level set methods and dynamic implicit surfaces, vol 153. Springer
Osher S, Sethian J (1988) Fronts propagating with curvature dependent speed: algorithms based on hamilton-jacobi formulations. J Comput Phys 79:12–49
Pasko A, Fryazinov O, Vilbrandt T, Fayolle PA, Adzhiev V (2011) Procedural function-based modelling of volumetric microstructures. Graph Models 73(5):165–181
Rao S (2009) Engineering optimization: theory and practice. Wiley
Rozvany G (1998) Exact analytical solutions for some popular benchmark problems in topology optimization. Struct Optim 15(1):42–48
Scilab Enterprises (2012) Scilab: free and open source software for numerical computation. Scilab Enterprises, Orsay. http://www.scilab.org
Sethian J (1999) Level set methods and fast marching methods: evolving interfaces in computational geometry, fluid mechanics, computer vision, and materials science, vol 3. Cambridge University press
Sigmund O (2000) A new class of extremal composites. J Mech Phys Solids 48(2):397–428
Sigmund O, Clausen PM (2007) Topology optimization using a mixed formulation: an alternative way to solve pressure load problems. Comput Methods Appl Mech Eng 196(13):1874–1889
Simar A, Brechet Y, De Meester B, Denquin A, Gallais C, Pardoen T (2012) Integrated modeling of friction stir welding of 6xxx series al alloys: Process, microstructure and properties. Progress Mater Sci 57(1):95–183
Sokolowski J, Zochowski A (1999) On the topological derivative in shape optimization. SIAM J Control Optim 37(4):1251–1272
Wang MY, Wang X (2004) Color level sets: a multi-phase method for structural topology optimization with multiple materials. Comput Methods Appl Mech Eng 193:469–496
Wang MY, Wang X (2005) A level-set based variational method for design and optimization of heterogeneous objects. Comput Aided Des 37(3):321–337
Wang MY, Zhou S (2004) Phase field: a variational method for structural topology optimization. Comput Model Eng Sci 6(6):547–566
Wang MY, Wang X, Guo D (2003) A level set method for structural topology optimization. Comput Methods Appl Mech Eng 192(1):227–246
Wang X, Mei Y, Wang MY (2004) Level-set method for design of multi-phase elastic and thermoelastic materials. Int J Mech Mater Des 1:213–239
Wolf D (1992) Materials interfaces: atomic-level structure and properties. Chapman & Hall
Wulff G (1901) Zur frage der geschwindigkeit des wachstums und der aufloesung der krystallflachen. Z Kryst 34:449–530
Xia Q, Wang MY (2008a) Simultaneous optimization of the material properties and the topology of functionally graded structures. Comput Aided Des 40(6):660–675
Xia Q, Wang MY (2008b) Topology optimization of thermoelastic structures using level set method. Comput Mech 42:837–857
Yin L, Ananthasuresh G (2002) A novel topology design scheme for the multi-physics problems of electro-thermally actuated compliant micromechanisms. Sensors Actuators A Phys 97:599–609
Zhou S, Wang M (2007) Multimaterial structural topology optimization with a generalized cahn–hilliard model of multiphase transition. Struct Multidiscip Optim 33(2):89–111